Universität Stuttgart

SimTech
Cluster of Excellence

Magnus Redeker · Bernard Haasdonk

A POD-EIM reduced two-scale model for crystal growth

{redeker,haasdonk}@mathematik.uni-stuttgart.de
Institute for Applied Analysis and Numerical Simulation, University of Stuttgart,
Pfaffenwaldring 57, 70569 Stuttgart, Germany.

Abstract Complex physical models depending on microstructures developing over time often result in simulation schemes that are very demanding concerning computational time. The two-scale model considered in the current presentation describes a phase transition of a binary mixture with the evolution of equiaxed dendritic microstructures. It consists of a macroscopic heat equation and a family of microscopic cell problems modeling the phase transition. Those phase transitions need to be resolved by very fine computational meshes leading to the demanding numerical complexity.

The current study presents a reduced version of this two-scale model. The reduction aims at accelerating the microscopic model, which is parametrized by the macroscopic temperature, while maintaining the accuracy of the detailed system. Parameter dependency, non-linearity, time-dependency, coupled field-variables and high solution complexity are challenging difficulties. They are addressed by a combination of several approaches: Proper Orthogonal Decomposition (POD), Empirical Interpolation Method (EIM) and a partitioning approach generating sub-models for different solution regimes. A new partitioning criterion based on feature extraction is applied.

The applicability of the reduction scheme is demonstrated experimentally: while the accuracy is largely maintained, the dimensionality of the detailed model and the computation time are reduced significantly.

Keywords Model reduction · Proper Orthogonal Decomposition · Empirical Interpolation · Parametrized two-scale model.

A POD-EIM reduced two-scale model
for crystal growth[*]

Magnus Redeker and Bernard Haasdonk

{redeker,haasdonk}@mathematik.uni-stuttgart.de

Institute for Applied Analysis and Numerical Simulation,
University of Stuttgart,
Pfaffenwaldring 57, 70569 Stuttgart, Germany.

Friday 6th June, 2014

Abstract

Complex physical models depending on microstructures developing over time often result in simulation schemes that are very demanding concerning computational time. The two-scale model considered in the current presentation describes a phase transition of a binary mixture with the evolution of equiaxed dendritic microstructures. It consists of a macroscopic heat equation and a family of microscopic cell problems modeling the phase transition. Those phase transitions need to be resolved by very fine computational meshes leading to the demanding numerical complexity.

The current study presents a reduced version of this two-scale model. The reduction aims at accelerating the microscopic model, which is parametrized by the macroscopic temperature, while maintaining the accuracy of the detailed system. Parameter dependency, non-linearity, time-dependency, coupled field-variables and high solution complexity are challenging difficulties. They are addressed by a combination of several approaches: Proper Orthogonal Decomposition (POD), Empirical Interpolation Method (EIM) and a partitioning approach generating sub-models for different solution regimes. A new partitioning criterion based on feature extraction is applied.

The applicability of the reduction scheme is demonstrated experimentally: while the accuracy is largely maintained, the dimensionality of the detailed model and the computation time are reduced significantly.

Keywords: Model reduction, Proper Orthogonal Decomposition, Empirical Interpolation, Parametrized two-scale model.

1 Introduction

Many technically relevant processes exhibit a priori unknown microstructures that evolve in time. Important examples are solidification processes with dendritic and eutectic microstructures [7, 27], flow in porous media with changing pore geometry as a consequence

---

[*]This presentation is dedicated to Prof. Christof Eck.

of elastoplastic deformations and deposition or desorption of matter, and microstructures in epitaxial growth of thin solid layers. Due to huge differences in relevant length and possibly also time scales, it is usually not feasible to simulate such processes by a direct numerical discretization of a full model. A much more promising approach is the usage of homogenization or averaging techniques, that were originally developed with the aim to find purely macroscopic models with suitable constitutive laws that model the properties of the microstructure [6, 20, 22]. The application of those methods to processes with evolution of a priori unknown microstructures typically leads to full two- or multi-scale models that combine differential equations on the smallest scales with homogenized differential equations on the macroscopic scales [36]. Both scales are coupled: the macroscopic fields influence the evolution of the microstructure, and the microscopic fields enter the homogenized equations via averaged coefficients. A direct discretization of such a model typically requires the solution of a full microscopic cell problem for every node of a macroscopic numerical grid. This leads to a huge numerical complexity and limits the application to problems with comparatively small macroscopic grids.

The present study presents a model reduction approach for a two-scale model for crystal growth. The procedure aims at the reduction of the microscopic model in order to accelerate the overall model. The problem poses several challenges for model reduction: parameter dependency via the macroscopic temperature, high dimensionality, several coupled field variables, time-dependency and non-linearity in the microscopic model. Correspondingly, several modern reduction strategies need to be combined. First, the high dimensionality of the microscopic model is addressed via a Proper Orthogonal Decomposition (POD) strategy [23, 35], i.e. snapshot-based generation of a low-dimensional approximation space and projection of the detailed microscopic model to this subspace. Different POD spaces for the different field variables are generated resulting in coupled reduced models. The non-linearity and parameter-dependency is addressed by the Empirical Interpolation Method (EIM) [2], which enables to efficiently evaluate local parametric discretization operators as in [5, 9]. Finally, the high solution complexity demands for partitioning approaches of the reduced models. This means, that not only one set of bases is generated, but several sets of reduced bases for different solution regimes. During the simulation a switching between these sub-models is realized by orthogonal projection. The criterion for partitioning is not time [8] nor some implicit partitioning [30, 37], but a partitioning according to a problem specific criterion that is obtained via a feature extraction of the present solution.

The reader is referred to other methods for the efficient solution of multi-scale models as e.g. [21, 31, 33] which are different to the current approach, which has some similarity to the method introduced in [32] using a database approach. In [32] the microscopic problems in the multi-scale model are replaced by simplified sample problems with prescribed macroscopic fields which are obtained by a global iterative procedure. Some further approaches of model reduction for multi-scale methods can be found in the literature, as the combination of these fields is currently a very active direction. Reduced basis approaches for cell problems in stationary two-scale problems have been presented in [3, 29]. A non-steady problem of polymeric flow involving macroscopic and microscopic models and their reduction has been shown in [25]. Projection-based approaches in the spirit of multi-scale FEM can also be found in [1, 24]. In contrast to these, the microscopic model considered here is a coupled nonlinear system, that requires more complex approximation procedures in order to obtain successful reduction. As mentioned before, this means different POD spaces for the different field variables and Empirical Interpolation addressing
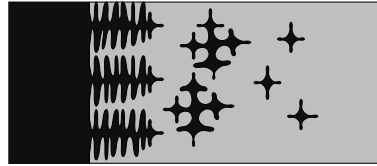
Figure 1.1: Columnar (on the left) and equiaxed dendritic structures, [12].

the non-linearity and parameter-dependency.

The organization of this article is as follows: Section 2 describes the detailed two-scale model to be solved, Section 3 introduces the reduced two-scale model, and finally Section 4 presents numerical results in two space dimensions which show the reduced model's efficiency.

2 The detailed two-scale model

Many solidification processes develop dendritic microstructures of equiaxed morphology as illustrated in Figure 1.1. Equiaxed structures grow from small solid kernels that nucleate in an undercooled melt. During solidification these kernels develop dendritic instabilities, for more details see e.g. [7] or [27]. To control these instabilities, models for dendritic growth must account for curvature undercooling and possibly also kinetic undercooling. The phenomenologically simplest model is the Stefan problem with Gibbs-Thomson effect, [34]. In contrast to the Stefan problem, a phase-field model approximates the sharp transition layer between the solid and the liquid phase by a diffuse phase transition region, [4]: the phase transition is described by a phase-field ϕ, which smoothly varies from its liquid value ϕ_ℓ to its solid value ϕ_s.

The detailed two-scale model is obtained by the application of a homogenization technique, under the assumption of fast heat diffusion and slow solute diffusion, to a microscopic model describing a solidification process of a binary mixture. The two-scale model consists of a macroscopic homogenized heat equation, and for each point of the macroscopic domain of a microscopic cell problem with periodic boundary conditions. For details see [10, 11, 13]. Well-posedness of the following continuous two-scale model (2.1), (2.3) and (2.4) is proven in Section 3 of [10]. Please note that the model considered here results from the model of [10] by the substitution $u = c + \phi$, the specifications $L = D_1 = -D_2 = 1$ and $K(\phi) = K \in \mathbb{R}$ and the commutation of the phase-field's liquid and solid value.

2.1 The macroscopic homogenized heat equation

The macroscopic heat equation in dimensionless form reads

$$\partial_t T - K \Delta T - \partial_t \overline{\phi}^Y = 0. \tag{2.1}$$

It is solved for the macroscopic temperature field $T = T(t, x)$ in the macroscopic time-space cylinder $Q = I_{t_{\text{end}}} \times \Omega$ consisting of the time interval $I_{t_{\text{end}}} = [0, t_{\text{end}}]$ and the macroscopic domain $\Omega \subset \mathbb{R}^2$. The averaged phase-field

$$\overline{\phi(t, x)}^Y = \tfrac{1}{|Y|} \int_Y \phi(t, x, y) \, dy \tag{2.2}$$
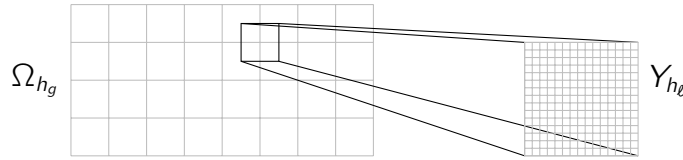
Figure 2.1: The macroscopic Ω_{h_g} and the local microscopic grid Y_{h_ℓ}.

depends on the microscopic cell problem in macroscopic point x, where Y denotes the microscopic cell domain; $\partial_t \overline{\phi(t,x)}^Y$ describes the averaged latent heat that is released during the phase transition from liquid to solid. The parameter K describes the heat conductivity, which is independent of the phase-field. The macroscopic equation is supplemented by a Neumann boundary condition and a constant initial temperature $T(0,x) = T_0$ for all $x \in \Omega$.

2.2 The microscopic cell problems

The microscopic cell problems describe the liquid-solid phase transition of a binary mixture. The governing equations in dimensionless form are

$$\partial_t u - \Delta_y u = \partial_t \phi, \tag{2.3}$$
$$\alpha \xi^2 \partial_t \phi - \xi^2 \Delta_y \phi + p'(\phi) - q(\nabla_y \phi, T, u, \phi) = 0. \tag{2.4}$$

The microscopic problem in a macroscopic point $x \in \Omega$ must be solved for the microscopic chemical potential $u = u(t,x,y)$ and the microscopic phase-field $\phi = \phi(t,x,y)$ on the time-space cylinder $I_{t_{\mathrm{end}}} \times \{x\} \times Y$, see Figure 2.1. It depends on the macroscopic temperature $T = T(t,x)$, hence the microscopic model is a parametrized model, where the macroscopic temperature represents the varying parameter. The phase-field ϕ varies smoothly from its liquid value -1 to its solid value 1. The equations are supplemented by Y-periodic boundary conditions for u and ϕ and initial conditions $u_0(y)$ for the chemical potential and $\phi_0(y)$ for the phase-field which are independent of the macroscopic grid point. The domain Y is a rectangle in $\mathbb{R}^2$. The function $p(\phi) = \frac{1}{2}\left(1 - \phi^2\right)^2$ is a double-well potential with minimum zero in ± 1. The function q triggers the dendritic growth and realizes the deviation from the equilibrium melting point,

$$
\begin{aligned}
q(\nabla_y \phi, T, u, \phi) = {} & 1.2\left(1 - \phi^2\right) \cdot \\
& \cdot \arctan\left(\tfrac{\xi}{1.2}(-u - T)\sigma_0\left(1 + \sigma_1\left(-1 + 2\left(2\tfrac{\|\nabla_y \phi\|_4^4}{\|\nabla_y \phi\|_2^4} - 1\right)\right)\right)\right).
\end{aligned}
\tag{2.5}
$$

The constants α, ξ, σ_0 and σ_1 are specified in Section 4.

The model does not include stochastic perturbations in the equations for the chemical potential. Such perturbations could trigger the side-branching into dendrites of second and higher order [26]. Therefore, the numerical results will only show four primary dendrites. In fact, the model is intended as a "simple" model case for the reduction scheme to be developed in Section 3.

2.3 The discretization of the two-scale model

The macroscopic as well as the microscopic problems are discretized with respect to the time by the Crank-Nicolson-method with a uniform time-step size $k_t := t_{\mathrm{end}}/K_t$ with total

step number K_t introducing the discrete time instants $t_n := nk_t, n = 0, \ldots, K_t$. With respect to the spatial discretization, standard second-order finite differences are used on uniform rectangular grids Ω_{h_g} and Y_{h_ℓ}, where $h_g = H_\ell h_\ell$ is the macroscopic and h_ℓ the microscopic mesh-size. Furthermore introduced is $\phi^n(y)$ as approximation of $\phi(t_n, x, y)$, where the x-dependency is suppressed for ease of the notation of the microscopic problem, and similarly $u^n(y)$, $T^n(x)$, $\overline{\phi^n(x)}^Y$ for $x = (x_0, x_1) \in \Omega_{h_g}, y = (y_0, y_1) \in Y_{h_\ell}$. The discrete phase-field equation reads

$$
\begin{aligned}
&\left(1 + \tfrac{2k_t}{\alpha h_\ell^2} + \tfrac{6k_t}{\alpha \xi^2} \left(\phi^n(y)\right)^2\right) \phi^{n+1}(y) - \tfrac{k_t}{2\alpha h_\ell^2}\textstyle\sum_{\overline{y}\in \overline{Y}_{h_\ell}(y)}\phi^{n+1}(\overline{y})\\
&= \left(1 - \tfrac{2k_t}{\alpha h_\ell^2} + \tfrac{2k_t}{\alpha \xi^2}\left(1 + 2\left(\phi^n(y)\right)^2\right)\right)\phi^n(y) + \tfrac{k_t}{2\alpha h_\ell^2}\textstyle\sum_{\overline{y}\in \overline{Y}_{h_\ell}(y)}\phi^n(\overline{y}) +\\
&\quad + \tfrac{k_t}{\alpha \xi^2} q(\nabla \phi^n(y),\, T^n,\, u^n(y),\, \phi^n(y)),
\end{aligned}
\tag{2.6}
$$

with the central node $y = (y_0, y_1)$ and its neighbors $\overline{Y}_{h_\ell}(y) = \{(y_0 + h_\ell, y_1), (y_0 - h_\ell, y_1), (y_0, y_1 + h_\ell), (y_0, y_1 - h_\ell)\}$, the discrete equation for the chemical potential

$$
\begin{aligned}
&\left(1 + \tfrac{2k_t}{h_\ell^2}\right) u^{n+1}(y) - \tfrac{k_t}{2h_\ell^2}\textstyle\sum_{\overline{y}\in \overline{Y}_{h_\ell}(y)}u^{n+1}(\overline{y})\\
&= \left(1 - \tfrac{2k_t}{h_\ell^2}\right) u^n(y) + \tfrac{k_t}{2h_\ell^2}\textstyle\sum_{\overline{y}\in \overline{Y}_{h_\ell}(y)}u^n(\overline{y}) + \left(\phi^{n+1}(y) - \phi^n(y)\right),
\end{aligned}
\tag{2.7}
$$

and the discrete equation for the temperature

$$
\begin{aligned}
&\left(1 + \tfrac{2k_t K}{h_g^2}\right) T^{n+1}(x) - \tfrac{k_t K}{2h_g^2}\textstyle\sum_{\overline{x}\in \overline{X}_{h_g}(x)}T^{n+1}(\overline{x})\\
&= \left(1 - \tfrac{2k_t K}{h_g^2}\right) T^n(x) + \tfrac{k_t K}{2h_g^2}\textstyle\sum_{\overline{x}\in \overline{X}_{h_g}(x)}T^n(\overline{x}) + \left(\overline{\phi^{n+1}(x)}^Y - \overline{\phi^n(x)}^Y\right),
\end{aligned}
\tag{2.8}
$$

with the central node $x = (x_0, x_1)$ and its neighbors $\overline{X}_{h_g}(x) = \{(x_0 + h_g, x_1), (x_0 - h_g, x_1), (x_0, x_1 + h_g), (x_0, x_1 - h_g)\}$. Stability considerations resp. linearization arguments yield the quadratic-term on the left-hand side of discretization (2.6), resulting from the approximation

$$
\begin{aligned}
p'(\phi) &\approx 2\left(\left(\phi^{n+1}\right)^3 - \phi^n\right) \approx 2\left(\left(\phi^n\right)^3 + 3\left(\phi^n\right)^2\left(\phi^{n+1} - \phi^n\right) - \phi^n\right)\\
&= 2\left(3\left(\phi^n\right)^2 \phi^{n+1} - 2\left(\phi^n\right)^2 - \phi^n\right).
\end{aligned}
\tag{2.9}
$$

The time discretization decouples the macroscopic and the microscopic problems: at first, in each time step, all microscopic problems are solved (at first the phase-field equation is solved and afterwards the equation for the chemical potential) with temperature data from the previous time step, then the macroscopic problem is solved.

As the microscopic model is reduced, a compactly written vector-matrix formulation is provided in the following, which is more accessible than the above detailed formulation. For this define $H := |Y_{h_\ell}|$ as the (high) dimension of the field variables of the microscopic model and introduce the vectors of degrees of freedom (DOF) $\underline{\phi}_H^n := (\phi^n(y))_{y\in Y_{h_\ell}}, \underline{u}_H^n := (u^n(y))_{y\in Y_{h_\ell}} \in \mathbb{R}^H$ assuming a suitable enumeration of Y_{h_ℓ}. First, for each given macroscopic temperature $T = T^n(x), x \in \Omega_{h_g}$ the phase-field is updated by determining $\underline{\phi}_H^{n+1}$ from

$$
\underline{L}_{\phi,H}(\underline{\phi}_H^n)\underline{\phi}_H^{n+1} = \underline{r}_H(\underline{\phi}_H^n, \underline{u}_H^n, T),
\tag{2.10}
$$

where $\underline{L}_{\phi,H} \in \mathbb{R}^{H \times H}$ is a matrix and $\underline{r}_H \in \mathbb{R}^{H \times 1}$ a vector which depend non-linearly on their arguments. Then, the chemical potential $\underline{u}_H^{n+1}$ is computed by

$$\underline{L}_{u,H} \underline{u}_H^{n+1} = \underline{F}_H u_H^n + (\underline{\phi}_H^{n+1} - \underline{\phi}_H^n), \tag{2.11}$$

where $\underline{L}_{u,H}, \underline{F}_H \in \mathbb{R}^{H \times H}$ are constant matrices. Hence, the potential problem will be simple to reduce, the phase-field model, however, will require more complex treatment.

3   The reduced two-scale model

This section develops a reduced version of the detailed two-scale model. Because the detailed macroscopic problem is by far not as hard to solve as the detailed microscopic problems, only the microscopic problems are reduced. Therefore, the reduced two-scale model consists of a detailed macroscopic problem for the temperature and reduced microscopic problems for the chemical potential and the phase-field.

The reduced model must account for the parameter dependency in the microscopic model (via the macroscopic temperature T in each point $x \in \Omega_{h_g}$), the nonlinearity on both sides of the microscopic phase-field equation (2.6) or rather (2.10), the time-dependency, i.e. good approximation of complete trajectories, a high solution variability as is expected in evolution of phase boundaries, and the coupling of the microscopic equations for the potential and the phase-field. To consider this, a POD for the trajectory treatment, EIM for the nonlinearity and parametrization and a partitioning approach to account for different solution regimes will be applied.

As typical in parametrized model reduction procedures, the overall reduction process consists of an offline and an online phase. In the offline phase, the reduced basis and further quantities are pre-computed, this phase is accepted to be costly, but only performed once. The online phase of the reduced model then will be of low order complexity and allows the reduced scheme to be used rapidly and multiply, i.e. for all macroscopic nodes and all times.

3.1   The offline phase

In the offline phase, all data required in the online phase has to be computed – a detailed description of the online phase follows in the sections 3.2 and 3.3. Therefore, the following steps are processed in the offline phase.

1. Solve the detailed two-scale model and collect snapshots
   (a) of the microscopic phase-field solution $\underline{\phi}_H^{n+1}$ of (2.6)/(2.10) to the set Π_ϕ,
   (b) of the microscopic solution of the chemical potential $\underline{u}_H^{n+1}$ of (2.7)/(2.11) to the set Π_u,
   (c) and of the right hand side $\underline{r}_{\phi,H}^n = \underline{r}_{\phi,H}^n(\underline{\phi}_H^n, \underline{u}_H^n, T^n)$ of equation (2.6)/(2.10) to the set Π_r.

   The choice of macroscopic nodes to draw trajectories from, and the sampling step width of the trajectories will be varied and specified in the experiments.

2. Construct two reduced bases by POD:
   (a) $\Phi_\phi = \{\varphi_{\phi,1}, \ldots, \varphi_{\phi,N_\phi}\} \subset \text{span}(\Pi_\phi)$ with size $N_\phi = |\Phi_\phi|$,
   (b) and $\Phi_u = \{\varphi_{u,1}, \ldots, \varphi_{u,N_u}\} \subset \text{span}(\Pi_u)$ with size $N_u = |\Phi_u|$.

For $\Delta = \phi, u$ and $i = 1, \dots, N_\Delta$, the N_Δ vectors $\varphi_{\Delta,i}$ are exactly the eigenvectors of the correlation operator of Π_Δ corresponding to the N_Δ largest eigenvalues. If the eigenvalues λ_i are sorted decreasingly, then N_Δ is the smallest number fulfilling the condition $\sum_{i=1,\dots,N_\Delta} \lambda_i \geq (1 - \epsilon_{POD}) \sum_{i=1,\dots,|\Pi_\Delta|} \lambda_i$ with a tolerance $0 < \epsilon_{POD} < 1$. The reader is referred to [23, 35] for further details on POD.

3. Perform the offline phase of the Empirical Interpolation Method (EIM) to generate an approximation of the microscopic phase-field model. The EIM [2, 28] approximates a function in an adaptive interpolation space: a Greedy algorithm constructs a suitable interpolation basis and identifies a set of interpolation points, the so-called 'magic points', [28]. Therefore, use as training data the snapshot set Π_r, define the tolerance $0 < \epsilon_{EI} < 1$, determine the indices $Y_M \subset Y_H$ of the magic points and generate the collateral basis Φ_ϕ^{EI}, cf. [5, 9]: training snapshots $\underline{L}_{\phi,H}\underline{\phi}_H^{n+1} - \underline{r}_H$ as required for the considered model are always zero, therefore snapshots of only $\underline{r}_H$ are used. Furthermore, with respect to the five-point-stencil which discretizes the spatial derivatives, determine the indices $Y_{N_M} \subset Y_H$ of the magic points' neighbors, but only of those neighbors which are not magic points themselves, i.e. $Y_M \cap Y_{N_M} = \emptyset$. Define $Y_M^\star = Y_M \cup Y_{N_M}$ and introduce an enumeration by $Y_M^\star(i) = Y_M(i)$ for all $i = 1, \dots, |Y_M|$ and $Y_M^\star(i) = Y_{N_M}(i - |Y_M|)$ for all $i = |Y_M| + 1, \dots, |Y_M| + |Y_{N_M}|$. The online phase of the Empirical Interpolation will be involved in the next sections.

4. Determine the reduced operators required for the solution of the reduced model; details on the operators are described in the following.

Although these offline quantities comprise two reduced bases and the interpolation points, this set of quantities is denoted a *reduced basis set* $\mathcal{B} = \{\Phi_\phi, \Phi_u, Y_M, Y_M^\star\}$.

Numerical results presented in Section 4 indicate that it is not practical to use only one basis set. Aim of the reduced model is on the one hand to obtain a solution in much less online time than needed for the detailed model, but, what is also important, on the other hand the reduced solution should be a good approximation of the detailed one. Therefore, as always, it is a competition between accuracy and cost of computation. Accuracy increases with increasing numbers N_ϕ, N_u and $|Y_M|$. Contrary to this relation, speed of computation increases with decreasing numbers N_ϕ, N_u, $|Y_M|$ and $|Y_{N_M}|$. In order to keep those numbers low but still to gain accurate results, it is advisable to use a partitioning approach to obtain multiple basis sets. Such procedures have been developed and applied successfully in literature. For example, a partitioning of the input parameter domain can be realized, e.g. via the hp-RB [14, 15, 16] or P-partitioning [18] approach. A partitioning of the time-axis can be applied to reduce complexity over time [8]. Also implicit partitioning approaches have been developed [30, 37] based on unsupervised learning approaches.

In this study, a problem-specific feature extraction is used to partitioning the solution space. This is a new conceptional contribution. The main principle of the partitioning strategy is in the offline phase to subdivide the set of snapshots into subsets with respect to a certain criterion and to construct from each subset one basis set. In the online phase a reduced solution is searched for in the span of a certain basis set if the solution of the previous time-step fulfills the distinguishing condition of that special basis set. The utilized criterion is the volume of the solid phases: the number of primary dendrites and their growth directions are prescribed by parameters, which as well as the initial condition are the same for all the microscopic problems, altogether they imply that microscopic solutions with similar solid phases' volumes also have similar shapes.

The proposed partitioning scheme is more suitable to the present application than the other schemes described above: a partitioning of the input parameter domain is inappropriate because the input parameter changes in time, therefore the input parameter domain consists of trajectories; a partitioning with respect to the time is unsuitable because the growth rate of a dendrite depends on the input parameter and therefore not explicitly on the time; it is the additional prior knowledge of volume growth that draws a distinction to unsupervised clustering procedures: as including prior knowledge is important in machine learning, the volume size is used as a distinctive feature characterizing solution regimes.

In the following the construction of the $N_{\mathcal{B}} \in \mathbb{N} \backslash \{0\}$ basis sets $\mathcal{B}_1, \ldots, \mathcal{B}_{N_{\mathcal{B}}}$ in the offline phase is explained. For every snapshot S_H that is collected while solving the detailed model, the corresponding volume $v_H(S)$ of the solid phase is determined, that is

$$v_H(S) = v_H(S(\phi_H^{n+1})) = \tfrac{1}{2} + \tfrac{1}{2H} \sum_{(y_0, y_1) \in Y_{h_\ell}} \phi_H^{n+1}(y_0, y_1). \tag{3.1}$$

Say $N_{S,\phi}$ is the total number of snapshots of the phase-field, $N_{S,u}$ of the chemical potential and $N_{S,r}$ of the right hand side. The volumes for the snapshot set Π_ϕ are ordered by size, the minimum $v_0 = \min_{S \in \Pi_\phi} v_H(S)$ as well as the maximum volume $v_{N_{\mathcal{B}}} = \max_{S \in \Pi_\phi} v_H(S)$ are determined, and for $i = 1, \ldots, N_{\mathcal{B}} - 1$ value v_i is equal to the $i \cdot \lfloor \frac{N_{S,\phi}}{N_{\mathcal{B}}} \rfloor$-th smallest volume. Then each of the snapshot-sets Π_ϕ, Π_u and Π_r is subdivided into $N_{\mathcal{B}}$ subsets $\Pi_{\phi,1}, \ldots, \Pi_{\phi,N_{\mathcal{B}}}$, $\Pi_{u,1}, \ldots, \Pi_{u,N_{\mathcal{B}}}$ and $\Pi_{r,1}, \ldots, \Pi_{r,N_{\mathcal{B}}}$ according to the following criterion

$$\Pi_{\Delta,i} = \{ S \in \Pi_\Delta \mid v_{i-1} - \epsilon_{\mathcal{B}}(v_{i-1} - v_{i-2}) \leq v_H(S) \leq v_i + \epsilon_{\mathcal{B}}(v_{i+1} - v_i) \} \tag{3.2}$$

for $i = 1, \ldots, N_{\mathcal{B}}$ and $\Delta = \phi, u, r$, with $v_{-1} = v_0$ and $v_{N_{\mathcal{B}}+1} = v_{N_{\mathcal{B}}}$ and $0 \leq \epsilon_{\mathcal{B}} < 1$. If $\epsilon_{\mathcal{B}}$ is zero, then all the subsets $\Pi_{\phi,i}$ have the same cardinal number. If $\epsilon_{\mathcal{B}}$ is larger than zero, then the intersection of two subsets $\Pi_{\phi,i}$ and $\Pi_{\phi,i+1}$ might contain more than only one snapshot. Allowing intersections pursues the objective to guarantee smooth transitions from one basis set to a neighboring one in the online phase. Finally, for $i = 1, \ldots, N_{\mathcal{B}}$ the basis sets $\mathcal{B}_i = (\Phi_{\phi,i}, \Phi_{u,i}, Y_{M,i}, Y_{M,i}^\star)$ are determined according to the steps 2.-4. from the subsets of snapshots $\Pi_{\phi,i}$, $\Pi_{u,i}$ and $\Pi_{r,i}$. The reason for the subdivision of the snapshots into subsets with similar cardinal numbers is the expectation that this results in similar cardinal numbers N_ϕ, N_u, $|Y_M|$ and $|Y_M^\star|$ for all the basis sets $\mathcal{B}_i$, $i = 1, \ldots, N_{\mathcal{B}}$. If the sizes of all basis sets are similar, then not only the accuracy but also the cost of computation is on the same level for the whole set of basis sets.

How the $N_{\mathcal{B}}$ basis sets $\mathcal{B}_1, \ldots, \mathcal{B}_{N_{\mathcal{B}}}$ are used to construct the reduced solutions in the online phase is explained in this paragraph. In the beginning of every time-step $n + 1$ the new i.e. appropriate basis set is determined, that is at first the volume $v_{N_\phi}^n$ of the solid phase is determined, for the old i.e. current basis set $\mathcal{B}_i$ that is

$$v_{N_\phi}^n = \tfrac{1}{2} + \tfrac{1}{2H} \begin{pmatrix} 1 & \cdots & 1 \end{pmatrix} \underline{\Phi}_{\phi,i} \underline{\phi}_{N_\phi,i}^n, \tag{3.3}$$

and if $v_{j-1} < v_{N_\phi}^n \leq v_j$ then $\mathcal{B}_j$ is the appropriate basis set. Contrary to the offline phase, it is $v_0 = -\infty$ and $v_{N_{\mathcal{B}}} = \infty$ in the online phase in order to capture all possible volume sizes, including those exceeding the training data range. If the current and the appropriate basis set differ, then the reduced solutions of the previous time-step n are orthogonally projected into the span of the appropriate basis set, that is

$$\underline{\phi}_{N_\phi,j}^n = \underline{\Phi}_{\phi,j}^\top \Phi_{\phi,i} \underline{\phi}_{N_\phi,i}^n, \qquad \underline{u}_{N_u,j}^n = \underline{\Phi}_{u,j}^\top \Phi_{u,i} \underline{u}_{N_u,i}^n, \tag{3.4}$$

where for $\Delta = \phi, u$ and $\ell = 1, \ldots, N_{\mathcal{B}}$ the columns of the matrix $\underline{\Phi}_{\Delta,\ell} \in \mathbb{R}^{H,N_{\Delta,\ell}}$ are equal to the DOF-vectors of the POD-basis $\Phi_{\Delta,\ell}$. Completing this, the current basis set turns from $\mathcal{B}_i$ to the appropriate $\mathcal{B}_j$.

If a reduced model with multiple basis sets instead of only one is used, then what must be determined additionally in the online phase is only the appropriate basis set and potentially the projection of the phase-field and the chemical potential, where the projection matrices $\underline{\Phi}_{\Delta,i\pm1}^{\top}\underline{\Phi}_{\Delta,i}$ are pre-computed in the offline phase. The volumes of the solid phases are computed anyway because they are parameters of the macroscopic problem.

3.2 The reduced model for the chemical potential

In the online phase, the reduced chemical potential $\underline{u}_{N_u}^{n+1} \in \mathbb{R}^{N_u,1}$ is determined by the following equation, which is simply a Galerkin projection of (2.7)/(2.11), i.e. multiplication by $\underline{\Phi}_u^{T}$ from the left and inserting the reduced quantities. As the system matrix is constant, the system can be inverted resulting in

$$\underline{u}_{N_u}^{n+1} = \left(\underline{\Phi}_u^{\top}\underline{L}_{u,H}\underline{\Phi}_u\right)^{-1}\underline{\Phi}_u^{\top}\left(\underline{F}_H\underline{\Phi}_u\underline{u}_{N_u}^n + \underline{\Phi}_\phi\left(\underline{\phi}_{N_\phi}^{n+1} - \underline{\phi}_{N_\phi}^n\right)\right), \tag{3.5}$$

where $\underline{\Phi}_u \in \mathbb{R}^{H,N_u}$ is the matrix with columns equal to the DOF-vectors of the current appropriate POD-basis Φ_u, and $\underline{\Phi}_\phi \in \mathbb{R}^{H,N_\phi}$ is the matrix with columns equal to the DOF-vectors of the current appropriate POD-basis Φ_ϕ.

The matrix operating on $\underline{u}_{N_u}^n$ as well as the matrix operating on the difference $\underline{\phi}_{N_\phi}^{n+1} - \underline{\phi}_{N_\phi}^n$ are constant for all times: they are pre-computed in the offline phase. Consequently, what remains to be computed in the online phase, in order to determine the reduced solution $\underline{u}_{N_u}^{n+1}$ of the chemical potential, are two small matrix vector products only.

3.3 The reduced model for the phase-field

The standard Empirical Interpolation system approximating the detailed system (2.6)/(2.10) for the phase-field reads

$$\underline{\Phi}_\phi^{EI}\underline{L}_{\phi,H}(\underline{\phi}_{N_\phi}^n)_{Y_M}\underline{\Phi}_\phi\underline{\phi}_{N_\phi}^{n+1} = \underline{\Phi}_\phi^{EI}\underline{r}_H(\underline{\phi}_{N_\phi}^n, \underline{u}_{N_u}^n, T)_{Y_M}, \tag{3.6}$$

with $\underline{L}_{\phi,H}(\underline{\phi}_{N_\phi}^n)_{Y_M} \in \mathbb{R}^{|Y_M|,H}$ and $\underline{r}_H(\underline{\phi}_{N_\phi}^n, \underline{u}_{N_u}^n, T)_{Y_M} \in \mathbb{R}^{|Y_M|,1}$, where the index Y_M denotes that only the rows belonging to the magic points' indices are considered. This system is not suitable because a high-dimensional system must be solved in the online phase and, furthermore, it is unknown whether the system is of full rank.

Therefore, $\underline{\Phi}_\phi^{EI}$ is eliminated from the equation by a suitable biorthogonal matrix multiplication, resulting in

$$\underline{L}_{\phi,Y_M}(\underline{\phi}_{N_\phi}^n)\underline{\phi}_{N_\phi}^{n+1} = \underline{r}_{Y_M}(\underline{\phi}_{N_\phi}^n, \underline{u}_{N_u}^n, T), \tag{3.7}$$

with a matrix $\underline{L}_{\phi,Y_M}(\underline{\phi}_{N_\phi}^n) \in \mathbb{R}^{|Y_M|,N_\phi}$, a vector $\underline{r}_{Y_M}(\underline{\phi}_{N_\phi}^n, \underline{u}_{N_u}^n, T) \in \mathbb{R}^{|Y_M|,1}$ and a scalar T which is the detailed macroscopic temperature solution of time-step n at the location of the microscopic problem in the macroscopic domain. This system is suitable because it is low-dimensional. It is solved for $\underline{\phi}_{N_\phi}^{n+1}$ by a Least-Squares procedure via the pseudoinverse, as it will be overdetermined in general.

In correspondence to (2.6)/(2.10), the matrix and the vector are defined as follows

$$\underline{L}_{\phi,Y_M}(\underline{\phi}^n_{N_\phi}) = \underline{L}(\underline{\phi}^n_{N_\phi})\underline{\tau}_{Y^\star_M}\Phi_\phi,$$
$$\underline{r}_{Y_M}(\underline{\phi}^n_{N_\phi}, \underline{u}^n_{N_u}, T^n) = \underline{R}\,\underline{\tau}_{Y^\star_M}\Phi_\phi\underline{\phi}^n_{N_\phi} + \underline{\hat{r}}_{Y_M}(\underline{\phi}^n_{N_\phi}, \underline{u}^n_{N_u}, T^n),$$

(3.8)

with $\underline{L}(\underline{\phi}^n_{N_\phi}) \in \mathbb{R}^{|Y_M|,|Y^\star_M|}$ defined as

$$\left(\underline{L}(\underline{\phi}^n_{N_\phi})\right)_{i,j} = \begin{cases} 1 + \frac{2k_t}{\alpha h_\ell^2} + \frac{6k_t}{\alpha\xi^2}\left(\left(\underline{\tau}_{Y_M}\Phi_\phi\underline{\phi}^n_{N_\phi}\right)_i\right)^2 & \text{for } j = i, \\ -\frac{k_t}{2\alpha h_\ell^2} & \text{if } Y^\star_M(j) \text{ is a neighbor of magic point } Y_M(i), \\ 0 & \text{otherwise,} \end{cases}$$

(3.9)

and $\underline{R} \in \mathbb{R}^{|Y_M|,|Y^\star_M|}$ defined as

$$\underline{R}_{i,j} = \begin{cases} 1 - \frac{2k_t}{\alpha h_\ell^2} + \frac{2k_t}{\alpha\xi^2} & \text{for } j = i, \\ \frac{k_t}{2\alpha h_\ell^2} & \text{if } Y^\star_M(j) \text{ is a neighbor of magic point } Y_M(i), \\ 0 & \text{otherwise,} \end{cases}$$

(3.10)

with the restriction-matrices $\underline{\tau}_{Y_M} \in \mathbb{R}^{|Y_M|,H}$ and $\underline{\tau}_{Y^\star_M} \in \mathbb{R}^{|Y^\star_M|,H}$ defined as

$$\left(\underline{\tau}_{Y_M}\right)_{i,j} = \begin{cases} 1 & \text{for } j = Y_M(i), \\ 0 & \text{otherwise,} \end{cases} \qquad \left(\underline{\tau}_{Y^\star_M}\right)_{i,j} = \begin{cases} 1 & \text{for } j = Y^\star_M(i), \\ 0 & \text{otherwise.} \end{cases}$$

(3.11)

and finally with

$$\left(\underline{\hat{r}}_{Y_M}(\underline{\phi}^n_{N_\phi}, \underline{u}^n_{N_u}, T^n)\right)_i = \frac{4k_t}{\alpha\xi^2}\left(\left(\underline{\tau}_{Y_M}\Phi_\phi\underline{\phi}^n_{N_\phi}\right)_i\right)^3 +$$
$$+ q\left(\left(\nabla_y\phi^\star\right)_i, T^n, \left(\underline{\tau}_{Y_M}\Phi_u\underline{u}^n_{N_u}\right)_i, \left(\underline{\tau}_{Y_M}\Phi_\phi\underline{\phi}^n_{N_\phi}\right)_i\right),$$

(3.12)

where $(\nabla_y\phi^\star)_{i,j}$ is the approximation of the j-th derivative of ϕ^n in the i-th magic point: without going into the details here, in order to obtain the j-th derivatives in the magic points simply a matrix-vector product must be computed, where the matrix is similar to the restriction matrix $\underline{\tau}_{Y^\star_M}$ and the vector is the former reduced solution.

Many of the products of the reduced system (3.7) are pre-computed in the offline phase, what still has to be computed in every time step $n+1$ in the online phase is

1. the matrix vector products of $\underline{\tau}_{Y_M}\Phi_\phi \in \mathbb{R}^{|Y_M|,N_\phi}$ and $\underline{\phi}^n_{N_\phi} \in \mathbb{R}^{N_\phi,1}$ as well as of $\underline{\tau}_{Y_M}\Phi_u \in \mathbb{R}^{|Y_M|,N_u}$ and $\underline{u}^n_{N_u} \in \mathbb{R}^{N_u,1}$ – in order to obtain the values of ϕ and u in the magic points,

2. the matrix vector products of $A_j\underline{\tau}_{Y^\star_M}\Phi_\phi \in \mathbb{R}^{|Y_M|,N_\phi}$ and $\underline{\phi}^n_{N_\phi} \in \mathbb{R}^{N_\phi,1}$ – in order to obtain the j-derivatives of ϕ in the magic points, with a suitable $A_j \in \mathbb{R}^{|Y_M|,|Y^\star_M|}$,

3. the first diagonal of matrix $\underline{L}(\underline{\phi}^n_{N_\phi}) \in \mathbb{R}^{|Y_M|,|Y^\star_M|}$ and the product of the two matrices $\underline{L}(\underline{\phi}^n_{N_\phi}) \in \mathbb{R}^{|Y_M|,|Y^\star_M|}$ and $\underline{\tau}_{Y^\star_M}\Phi_\phi \in \mathbb{R}^{|Y^\star_M|,N_\phi}$ – in order to obtain the left-hand side matrix $\underline{L}_{\phi,Y_M}(\underline{\phi}^n_{N_\phi})$ of (3.7),

4. the product of $\underline{R}\,\underline{\tau}_{Y^\star_M}\Phi_\phi \in \mathbb{R}^{|Y_M|,N_\phi}$ and $\underline{\phi}^n_{N_\phi} \in \mathbb{R}^{N_\phi,1}$, the vector $\underline{\hat{r}}_{Y_M}(\underline{\phi}^n_{N_\phi}, \underline{u}^n_{N_u}, T^n) \in \mathbb{R}^{|Y_M|,1}$, and the sum of these two vectors – in order to obtain the right hand side vector $\underline{r}_{Y_M}(\underline{\phi}^n_{N_\phi}, \underline{u}^n_{N_u}, T^n)$ of (3.7),

5. and finally, the Least-Squares solution $\underline{\phi}_{N_\phi}^{n+1} \in \mathbb{R}^{N_\phi,1}$ of (3.7).

All of these computations for the online phase of the reduced models are completely independent of the high dimension H. The computational complexity only scales with $N_\phi, N_u, |Y_M|$ and $|Y_M^\star|$. This is true for the reduced systems, but also for the projection operations for a basis set change and the averaging procedure for coupling into the macroscopic temperature equation. Consequently, the reduced model provides an ideal offline-online decomposition.

4 Numerical results

In order to evaluate the reduced two-scale model's quality, this section presents the results of numerical computations. In particular compared are reduced to detailed numerical results. At first in order to show that the reduced model features a possible reproduction of detailed results, the detailed and the reduced solution are compared for a setting with a small time-space cylinder. In a second step, on a larger time-space cylinder, it is shown that the reduced model not only produces accurate results but also speeds up the computation significantly. And finally in a third step, generalization abilities of the reduced model are investigated.

This paragraph defines the different detailed models to be solved or to be approximated by reduced models in the following subsections. Equations (2.6)/(2.10) and (2.7)/(2.11) describe the microscopic model to be solved on the microscopic domain $Y_{h_\ell} = [0, H_\ell h_\ell]^2$ with space increment $h_\ell = 0.005$, and the macroscopic heat equation (2.8) is to be solved on the macroscopic domain $\Omega_{h_g} = [0, H_{g,1} h_g] \times [0, H_{g,2} h_g]$ with space increment $h_g = H_\ell h_\ell$. Therefore, Ω_{h_g} consists of $(H_{g,1}+1) \cdot (H_{g,2}+1)$ nodes, each of them governing one microscopic problem on Y_{h_ℓ} consisting of $(H_\ell + 1)^2$ nodes. The computation time is from 0 to $K_t k_t$ with time increment $k_t = 2e\text{-}6$. On the macroscopic scale, the effective heat conductivity K is larger than zero, and the boundary conditions of the heat equation are the prescribed heat fluxes

$$\frac{k_t K}{2h_g^2} \nabla T \cdot n = \begin{cases} -2c_{\text{boundary-flux}} & \text{for } x_1 = 0, \\ -c_{\text{boundary-flux}} & \text{for } x_2 = 0, \qquad c_{\text{boundary-flux}} > 0. \\ 0 & \text{otherwise,} \end{cases} \tag{4.1}$$

Put more simply, two parts of the boundary have cooling conditions, and the remaining two parts are isolated. For the microscopic cell problems the boundary conditions are periodic. The initial temperature T, the initial chemical potential u and the initial phase-field ϕ are for all $x \in \Omega_{h_g}$ and for all $y \in Y_{h_\ell}$ specified as

$$\begin{aligned} T(0,x) &= -0.1, \\ u(0,x,y) &= -0.1, \\ \phi(0,x,y) &= \tanh\left(0.25\left(\sqrt{\sum_{i=1,2}\left(\frac{1}{h_\ell}y_i - \frac{H_\ell}{2}\right)^2} - 5\right)\right). \end{aligned} \tag{4.2}$$

By reason that the initial conditions of the microscopic unknowns u and ϕ are independent of their location on the macroscopic domain, they are equal for all the microscopic problems. Furthermore, they (in combination with the initial temperature condition) imply

that, initially, a small solid kernel occupies the center of every microscopic domain and that each kernel is surrounded by an undercooled melt. The microscopic physical parameters are specified as $\alpha = 5$, $\xi = 0.01$, $\sigma_0 = 5000$ and $\sigma_1 = 0.5$. Consequently, the different models to be solved differ only in the following variables: the number of microscopic nodes $H_\ell > 0$ in both dimensions, the number of macroscopic nodes $H_{g,1} > 0$ in the first and $H_{g,2} > 0$ in the second dimension, the number of time-steps $K_t > 0$, the macroscopic boundary temperature outflow-constant $c_{\text{boundary-flux}} > 0$ and the macroscopic heat conductivity $K > 0$.

A reduced solution's accuracy is estimated by comparing its macroscopic temperature solution T_{red} to the detailed method's temperature solution T_{det}. The error $\Delta T := |T_{\text{red}} - T_{\text{det}}|$ is measured in the discrete L_2- and L_∞-norms on the discrete macroscopic space domain Ω_{h_g} or on the whole discrete time-space cylinder $Q_{k_t, h_g} = I_{t_{\text{end}}, k_t} \times \Omega_{h_g}$:

$$
\begin{aligned}
\|\Delta T(t_n, \cdot)\|_{\Omega, 2} &= \sqrt{\tfrac{1}{|\Omega_{h_g}|} \sum_{x \in \Omega_{h_g}} |\Delta T(t_n, x)|^2}, \\
\|\Delta T(\cdot, \cdot)\|_{Q, 2} &= \sqrt{\tfrac{1}{N+1} \sum_{n=0}^{N} \|\Delta T(t_n, \cdot)\|_{\Omega, 2}^2}, \\
\|\Delta T(t_n, \cdot)\|_{\Omega, \infty} &= \max_{x \in \Omega_{h_g}} |\Delta T(t_n, x)|, \\
\|\Delta T(\cdot, \cdot)\|_{Q, \infty} &= \max_{n=0, \dots, N} \|\Delta T(t_n, \cdot)\|_{\Omega, \infty}.
\end{aligned}
\tag{4.3}
$$

Unfortunately, a small temperature-error is only a necessary but not a sufficient condition for a good reduced approximation of the detailed microscopic solution. Therefore, if a reduced solution with a small temperature-error exists, then also the errors of the microscopic reduced solutions are measured in the discrete L_∞-/L_2-norm in the discrete microscopic time-space cylinder $Q^\star = I_{t_{\text{end}}, k_t} \times \Omega_{h_g}^\star \times Y_{h_\ell}$, where $\Omega_{h_g}^\star$ represents only the four nodes in the corners of the macroscopic domain, which are $(0, 0)$, $(H_{g,1}, 0)$, $(0, H_{g,2})$ and $(H_{g,1}, H_{g,2})$. Evaluating all microscopic solutions would require an enormous amount of memory, therefore only the solutions in the corners are evaluated. Furthermore, in the subsections 4.2 and 4.3 with large time-space cylinders, the microscopic solutions are evaluated only every 50 steps in time. Still, this evaluation-strategy seems not to be too unreasonable because, due to the macroscopic boundary conditions, macroscopic corner node $(0, 0)$ records the lowest and $(H_{g,1}, H_{g,2})$ the highest temperature in every time-step, and therefore the microscopic solutions characterized by the largest and the smallest dendrite are evaluated. The two remaining corner nodes represent dendrites in between.

4.1 Results on a small time-space cylinder

The detailed two-scale model to be solved in this subsection is completed by the following set of parameters: $H_\ell = 50$, $H_{g,1} = 10$, $H_{g,2} = 5$, $K_t = 50$, $c_{\text{boundary-flux}} = 2e\text{-}3$ and $K = 2000$. This model-setting is designed in order to test only whether the reduced model is capable of reproducing detailed results. The other important feature of reduced models, the increase of computational speed is, alongside of accuracy of course, a topic of the next subsection. Figure 4.1 illustrates the detailed model's macroscopic temperature solution, its microscopic phase-field solution in the macroscopic node $(0, 0)$ and the evolutions of the volumes of the solid phases in the macroscopic corners nodes.

The reduced models to be evaluated in the following are constructed from snapshots produced by the detailed solution with snapshot-time-increment $s_t = 1$, that is every microscopic solution participates in their construction. For 50 microscopic problems and

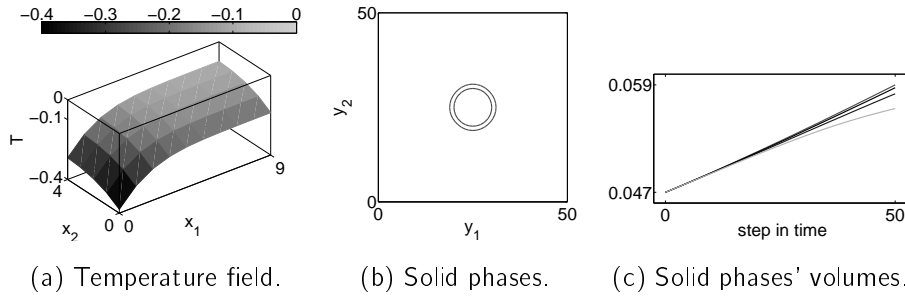(a) Temperature field.   (b) Solid phases.   (c) Solid phases' volumes.

Figure 4.1: Results of the detailed two-scale model on the small time-space cylinder. Figure (a) depicts the macroscopic temperature field in the end. Figure (b) presents the initial (inner circle) and the final solid phase in the macroscopic node $(0,0)$. Figure (c) illustrates the evolution of the volumes of the solid phases in the macroscopic corner-nodes $(0,0)$, $(0,4)$, $(9,0)$ and $(9,4)$, listed from largest to smallest volume.

$(\epsilon_{POD}, \epsilon_{EI})$	N_ϕ	N_u	$|Y_M|$	$|Y_M^\star|$	$\|\Delta T\|_{Q,\infty}$	$\|\Delta T\|_{Q,2}$
$(1e\text{-}4, 1e\text{-}4)$	2	3	14	46	3.38e-3	1.96e-3
$(1e\text{-}5, 1e\text{-}5)$	2	4	23	58	4.03e-3	2.78e-3
$(1e\text{-}6, 1e\text{-}6)$	3	5	28	63	2.58e-3	5.94e-4
$(1e\text{-}10, 1e\text{-}10)$	9	14	58	112	1.20e-5	2.41e-6
$(1e\text{-}14, 1e\text{-}4)$	21	30	14	46	7.81e-2	7.13e-2
$(1e\text{-}14, 1e\text{-}5)$	21	30	23	58	1.32e-7	3.34e-8
$(1e\text{-}14, 1e\text{-}6)$	21	30	28	63	2.69e-7	6.31e-8
$(1e\text{-}14, 1e\text{-}10)$	21	30	58	112	1.34e-7	1.90e-8
$(1e\text{-}14, 1e\text{-}14)$	21	30	114	251	2.35e-8	4.10e-9

Table 4.1: Results of reduced two-scale models on the small time-space cylinder. The reduced models are characterized by one basis set and varying tolerances ϵ_{POD} and ϵ_{EI}.

50 steps in time this results in 2500 snapshots of the phase-field, of the chemical potential and of the right-hand side.

Table 4.1 presents results for reduced models consisting of one basis set only for varying tolerances ϵ_{POD} and ϵ_{EI}. For a diminishing ϵ_{POD}, the tolerance that influences the construction of the POD-bases for ϕ and u, the sizes N_ϕ and N_u of the two bases Φ_ϕ and Φ_u increase, of course. Certainly as well, for a diminishing ϵ_{EI} the number of the magic points $|Y_M|$ increases. Also increasing is the number $|Y_M^\star|$: for larger tolerances it is nearly a factor of five in $|Y_M|$ versus $|Y_M^\star|$, which is caused by the five-star finite difference discretization; for smaller tolerances many of the magic points' neighbors are magic themselves. The error results imply that it is not necessary to use tolerances ϵ_{POD} and ϵ_{EI} of the same order. But, comparing the results for $(\epsilon_{POD}, \epsilon_{EI}) = (1e\text{-}4, 1e\text{-}4)$ and $(\epsilon_{POD}, \epsilon_{EI}) = (1e\text{-}14, 1e\text{-}4)$, in order to produce accurate reduced results, the size of the POD-basis for the phase-field N_ϕ must not be larger than the number of the magic nodes $|Y_M|$. This is due to the fact that the system of linear equations (3.7) for the reduced phase-field is under-determined for $N_\phi > |Y_M|$. What is of great importance and what justifies the reduced model, is that, disregarding some insignificant deviations, for diminishing tolerances the errors decrease: the reduced model is capable of at least reproducing the detailed macroscopic temperature solution.

Table 4.2 presents results for reduced models consisting of a variable number of basis

$(N_{\mathcal{B}}, \epsilon_{\mathcal{B}})$	N_ϕ	N_u	$|Y_M|$	$|Y_M^\star|$	$\|\Delta T\|_{Q,\infty}$	$\|\Delta T\|_{Q,2}$
$(1, -)$	21	30	114	251	2.35e-8	4.10e-9
$(2, 0.1)$	16.50	24.00	93.50	212.00	5.53e-8	2.24e-8
$(4, 0.1)$	13.75	19.50	81.00	174.75	2.78e-7	7.68e-8
$(10, 0)$	10.90	15.20	66.60	146.10	1.86e-6	1.15e-6
$(10, 0.1)$	11.30	15.50	68.70	151.20	3.92e-7	1.30e-7
$(10, 0.2)$	11.60	15.90	69.90	153.60	2.51e-7	6.28e-8
$(10, 0.5)$	12.50	17.50	74.80	163.50	1.34e-7	5.50e-8
$(10, 1)$	13.80	19.30	80.90	178.40	8.60e-8	4.30e-8
$(20, 0.1)$	10.10	13.95	58.75	128.25	2.98e-6	1.43e-6

Table 4.2: Results of reduced two-scale models on the small time-space cylinder. The reduced models are characterized by $\epsilon_{POD} = \epsilon_{EI} = $ 1e-14, a varying number of basis sets $N_{\mathcal{B}}$ and a varying tolerance $\epsilon_{\mathcal{B}}$. If a reduced model consists of more than one basis set, then the numbers N_ϕ, N_u, $|Y_M|$ and $|Y_M^\star|$ present the average sizes of all basis sets.

$(N_{\mathcal{B}}, \epsilon_{POD}, \epsilon_{EI})$	$\|\Delta T\|_{Q,\infty}$	$\|\Delta T\|_{Q,2}$	$\|\Delta\phi\|_{Q^\star,\infty}$	$\|\Delta\phi\|_{Q^\star,2}$	$\|\Delta u\|_{Q^\star,\infty}$	$\|\Delta u\|_{Q^\star,2}$
$(1, 1e\text{-}5, 1e\text{-}5)$	4.03e-3	2.78e-3	2.14e-2	5.82e-3	1.27e-2	5.88e-3
$(1, 1e\text{-}14, 1e\text{-}5)$	1.32e-7	3.34e-8	4.11e-6	1.72e-7	3.73e-6	1.38e-7
$(1, 1e\text{-}14, 1e\text{-}14)$	2.35e-8	4.10e-9	3.41e-6	8.69e-8	2.12e-6	5.54e-8
$(2, 1e\text{-}14, 1e\text{-}14)$	5.53e-8	2.24e-8	2.37e-6	1.27e-7	1.30e-6	9.99e-8
$(4, 1e\text{-}14, 1e\text{-}14)$	2.78e-7	7.68e-8	3.52e-6	4.82e-7	2.47e-6	4.54e-7
$(10, 1e\text{-}14, 1e\text{-}14)$	3.92e-7	1.30e-7	7.82e-6	7.51e-7	5.60e-6	7.26e-7
$(20, 1e\text{-}14, 1e\text{-}14)$	2.98e-6	1.43e-6	1.81e-5	2.77e-6	1.02e-5	2.73e-6

Table 4.3: Results of reduced two-scale models on the small time-space cylinder. The reduced model is characterized by varying parameters $N_{\mathcal{B}}$, ϵ_{POD} and ϵ_{EI}. In case of multiple basis sets it is $\epsilon_{\mathcal{B}} = 0.1$.

sets and a varying tolerance $\epsilon_{\mathcal{B}}$, with smallest tolerances $\epsilon_{POD} = \epsilon_{EI} = $ 1e-14. For constant $\epsilon_{\mathcal{B}}$ but an increasing $N_{\mathcal{B}}$ the average sizes N_ϕ, N_u, $|Y_M|$ and $|Y_M^\star|$ of the basis sets decrease, but unfortunately also the accuracy. The last observation can be explained by the constant tolerance $\epsilon_{\mathcal{B}}$: the larger the number of basis sets, the smaller the intersection of the basis sets, and therefore the larger the projection errors. Increasing $\epsilon_{\mathcal{B}}$ yields an increasing accuracy. At first sight it is surprising that the error of $(N_{\mathcal{B}}, \epsilon_{\mathcal{B}}) = (10, 1)$ is larger than for example of $(N_{\mathcal{B}}, \epsilon_{\mathcal{B}}) = (2, 0.1)$, but this may explained with projection errors: in case of only a few basis sets with a small $\epsilon_{\mathcal{B}}$, the projection error may be smaller than for the case with a larger $N_{\mathcal{B}}$ and a larger $\epsilon_{\mathcal{B}}$, but in the latter case the errors add up for each change of the basis set. Still, because the error is not significantly larger for models with a larger number of basis sets, and because the online computation time decreases significantly for decreasing sizes of the basis sets, therefore it is the reduced models with multiple basis sets that are more suitable for situations with larger time-space cylinders.

As mentioned before, small temperature errors are only a necessary condition for a good reduced approximation of the detailed microscopic solution. Therefore, Table 4.3 documents the errors of the microscopic solutions for some reduced models: as could be expected in view of the excellent overall macroscopic temperature approximation, the tighter the tolerances the smaller also the microscopic errors.

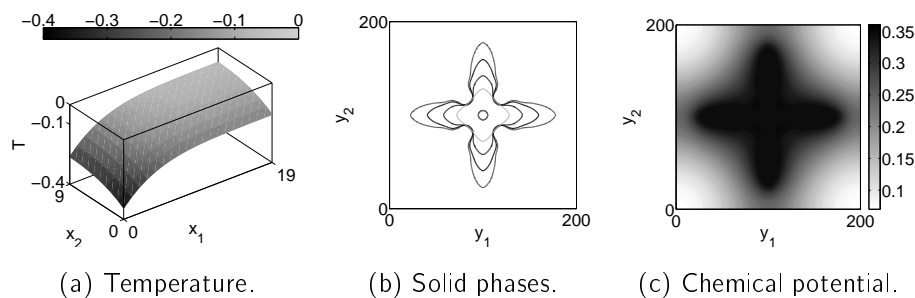(a) Temperature.   (b) Solid phases.   (c) Chemical potential.

Figure 4.2: Results of the detailed two-scale model on the large time-space cylinder. Figure (a) depicts the macroscopic temperature field in the end, Figure (b) presents the initial (inner circle) and the final solid phases in the macroscopic corner nodes $(0,0)$ (largest), $(0,9)$ (second-largest), $(19,0)$ (third-largest) and $(19,9)$, and Figure (c) shows the final microscopic chemical potential in $(0,0)$.

This subsection showed that the reduced model is capable of reproducing the detailed solution. The next subsection will show that the reduced model also produces accurate results on a larger time-space cylinder. Besides that, it will also show that the reduced model can be solved much more efficiently than the detailed one.

4.2   Results on a large time-space cylinder

The detailed two-scale model to be solved in this subsection is completed by the parameters $H_\ell = 200$, $H_{g,1} = 20$, $H_{g,2} = 10$, $K_t = 50000$, $c_{\text{boundary-flux}} = 5e\text{-}6$ and $K = 200$. Therefore, this setting, called setting S_0, is characterized by a larger time-space cylinder than the previous subsection's setting. Figure 4.2 illustrates the result of the detailed two-scale model. Because of the boundary conditions it is always the macroscopic corner $(0,0)$ which records the lowest temperature and therefore the largest solid.

A reduced model is constructed from snapshots which are produced by the detailed model's solution. In course of the detailed simulation 10,000,000 microscopic problems are solved ($50,000$ time-steps times 200 macroscopic nodes). What is done in order to pre-select the snapshots that are utilized in a reduced model's construction, is that the detailed two-scale model is solved adaptively. The interested reader is referred to [31] for details on the adaptive solution strategy. Fundamental to it is the fact that microstructures develop similar features if they are influenced by similar temperature evolutions. Consequently, a microscopic solution can be approximated by the solution of another microscopic problem if the problems are influenced by similar temperature evolutions. Exercising this observation, the strategy selects microscopic problems to be solved and approximates the remaining problems' solutions.

The applied adaptive strategy is characterized by the following parameters: $\lambda = 0.1$, $c_{\text{tol}_c} = 0.2$, $c_{\text{tol},0} = 0$, $c_{\text{tol}_e} = 0.01$, RU=0, $eC = 1$, $M_A = 2$, IT-CA, $N_A(0) = (0,0)$, the Copy Method and a refining tolerance parameter $c_{\text{tol}_r,1} = 0.01$. The last parameter is straight proportional to the maximum distance of an approximated and at least one solved microscopic problem's influencing temperature evolution: the smaller it is the more microscopic problems are solved. Without going into details, the choice $c_{\text{tol}_r,1} = 0.01$ is a good compromise between cost of detailed offline computation and reduced online accuracy: on average 52.18 microscopic problems are solved per time-step, topping out at

	detailed solution	$(25, 1e\text{-}14, 1e\text{-}6)$	$(25, 1e\text{-}13, 1e\text{-}6)$	$(25, 1e\text{-}13, 1e\text{-}5)$	$(25, 1e\text{-}12, 1e\text{-}4)$	$(50, 1e\text{-}13, 1e\text{-}5)$	$(100, 1e\text{-}13, 1e\text{-}5)$	$(200, 1e\text{-}13, 1e\text{-}5)$
$t_{on}((0,0))$	1595	0.73	1.27	1.46	2.61	3.57	8.14	12.66
$t_{on}((19,0))$	1479	1.40	2.68	3.23	6.46	5.03	7.78	10.80
$t_{on}((0,9))$	1536	0.88	1.57	1.84	3.48	3.94	7.84	10.59
$t_{on}((19,9))$	1347	1.89	3.74	4.86	9.62	7.13	12.03	14.97
$\overline{t_{on}}$	1489.25	1.04	1.89	2.24	4.20	4.51	8.58	11.96
N_ϕ	-	81.16	60.84	60.84	48.04	49.16	41.60	36.93
N_u	-	68.04	49.12	49.12	39.32	40.46	34.86	31.25
$\lvert Y_M \rvert$	-	124.48	124.48	89.72	58.88	70.84	59.22	51.24
$\lvert Y_M^\star \rvert$	-	304.40	304.40	254.04	194.44	216.26	191.34	172.38
$\lVert \Delta T \rVert_{Q,\infty}$	-	7.12e-6	9.02e-6	1.29e-5	1.18e-3	4.56e-5	6.08e-5	4.77e-4
$\lVert \Delta T \rVert_{Q,2}$	-	4.28e-7	1.02e-6	1.62e-6	1.52e-5	1.51e-6	2.15e-6	4.49e-6

Table 4.4: *Run-time and speed-up results on the large time-space cylinder. The reduced models are characterized by the common parameter $\epsilon_\mathcal{B} = 0.1$ and the varying parameter set $(N_\mathcal{B}, \epsilon_{POD}, \epsilon_{EI})$. For the detailed solution the value $t_{on}(x)$ represents the time in seconds that one Intel(R) Xeon(R) CPU E7- 4830 @ 2.13GHz needs to solve the microscopic problem in the time-space cylinder $I_{t_{end}, k_t} \times \{x\} \times Y_{h_\ell}$, and $\overline{t_{on}}$ represents the average time. For the reduced solutions, which are computed on the same CPU, it is not the absolute time but the speed-up compared to the detailed solution that is presented.*

77, resulting in an adaptive offline temperature solution with the errors $\lVert \Delta T \rVert_{Q,\infty} = 3.35e\text{-}4$ and $\lVert \Delta T \rVert_{Q,2} = 8.93e\text{-}5$ compared to the non-adaptive detailed solution.

The ultimate objective is to construct a (non-adaptive) reduced model which is a good approximation of the (non-adaptive) detailed model, desirably an even better approximation than the adaptive solution whose snapshots are used to construct the reduced model. Again without going into details, numerical results indicate that it is not suitable to produce snapshots with a constant time-step-increment s_t: for an oversized s_t the accuracy especially in the very beginning (due to rapid changes in the initially constant chemical potential) is weak, on the other hand the smaller s_t the more memory is needed. In fact a reasonable compromise is the increasing snapshot-increment s_t^i: until the 100-th time-step the increment is 1, then until the 200-th it is 2, until the 500-th 5, until the 1000-th 10, until the 2000-th 25, and afterwards 50. Therefore, 53974 (i.e. around 0.5% of all possibly computed) microscopic solutions are used to construct the reduced models presented and evaluated in the following.

Table 4.4 states the time needed to solve the microscopic problems in the macroscopic corner nodes for the detailed and some reduced models, the sizes of the basis sets and the temperature error of the reduced solutions. Certainly, the tighter the tolerances ϵ_{POD} and ϵ_{EI} and the smaller the number of basis sets, the more time is needed to solve the reduced model but also the more accurate are the solutions. A good compromise for efficiency is the reduced model consisting of 100 basis sets which was constructed with respect to the
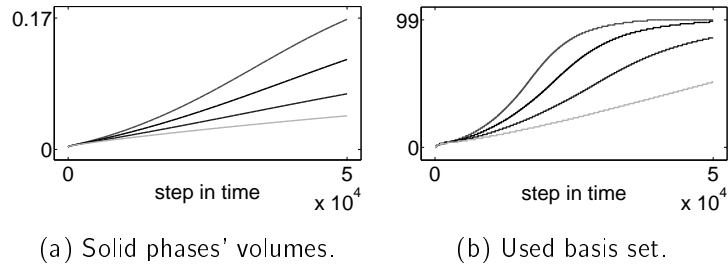
(a) Solid phases' volumes.   (b) Used basis set.

Figure 4.3: Results on the large time-space cylinder of the reduced model with parameters $N_B = 100$, $\epsilon_{POD} = 1e\text{-}13$, $\epsilon_{EI} = 1e\text{-}5$ and $\epsilon_B = 0.1$. Figure (a) illustrates the evolution of the solid phases' volumes and (b) the evolution of the utilized basis sets, both in the macroscopic corner nodes.

(a) Offline: error T.   (b) Offline: error ϕ.   (c) Offline: error u.

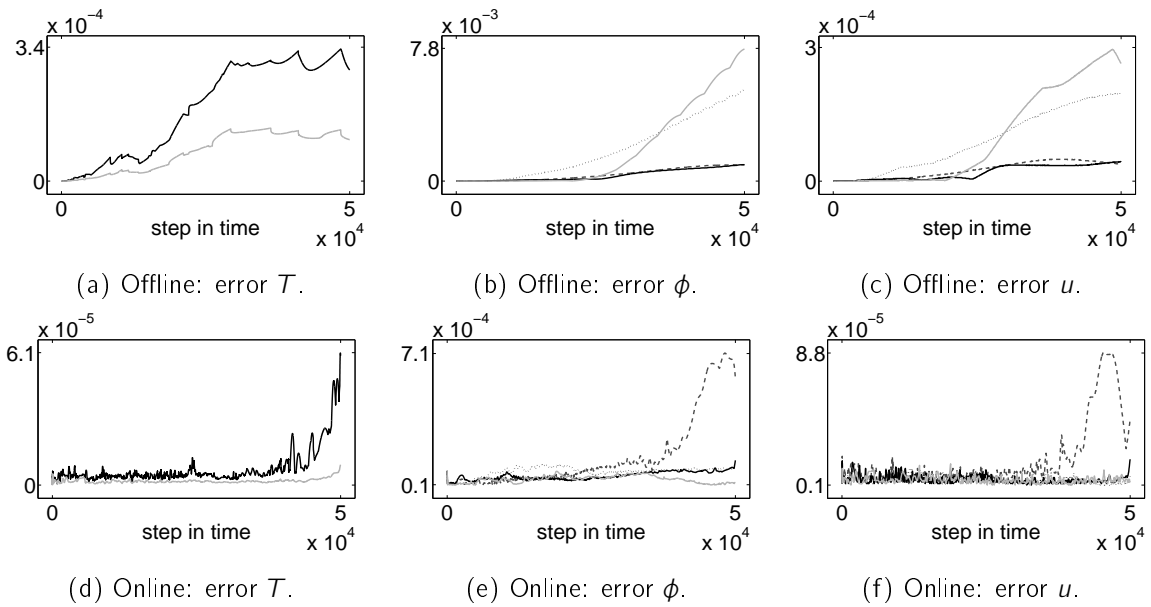(d) Online: error T.   (e) Online: error ϕ.   (f) Online: error u.

Figure 4.4: Results on the large time-space cylinder. Figures (a)-(c) depict results of the detailed adaptive model and Figures (d)-(f) results of the reduced non-adaptive model with parameters $N_B = 100$, $\epsilon_{POD} = 1e\text{-}13$, $\epsilon_{EI} = 1e\text{-}5$ and $\epsilon_B = 0.1$; the reduced model is constructed from the detailed adaptive solution. Figures (a) and (d) illustrate the respective $L_\infty(\Omega)$- (dark-gray) and $L_2(\Omega)$-error of the temperature solutions compared to the non-adaptive detailed solution. Figures (b) and (e) show the respective $L_\infty(Y)$-errors of the microscopic phase-fields in the macroscopic corner nodes and (c) and (f) of the microscopic chemical potentials in the macroscopic corner nodes $(0, 0)$ (dashed), $(19, 0)$ (dotted), $(0, 9)$ (dark-gray) and $(19, 9)$.

tolerances $\epsilon_{POD} = 1e\text{-}13$, $\epsilon_{EI} = 1e\text{-}5$ and $\epsilon_B = 0.1$: compared to the detailed solution the microscopic problems are solved 8.5 times faster on average but the maximum error of the temperature is only 6.08e-5. For this reduced model Figure 4.3 illustrates how the growth of the volume of a solid phase affects the utilized basis set building the reduced solution: the larger the volume the larger the index of the utilized basis set. Also for this model Figure 4.4 depicts its solution's error compared to the non-adaptive detailed solution. The error of the temperature is small in the beginning but it increases rapidly in the very end of the time-interval. Approximately the same holds for the error of the microscopic phase-

	$(25, 1e\text{-}14, 1e\text{-}6)$	$(25, 1e\text{-}13, 1e\text{-}6)$	$(25, 1e\text{-}13, 1e\text{-}5)$	$(25, 1e\text{-}12, 1e\text{-}4)$	$(50, 1e\text{-}13, 1e\text{-}5)$	$(100, 1e\text{-}13, 1e\text{-}5)$	$(200, 1e\text{-}13, 1e\text{-}5)$
Overall	$14.00\,h$	$11.72\,h$	$7.41\,h$	$5.18\,h$	$4.72\,h$	$5.24\,h$	$7.40\,h$
SubdivSnaps	1.80 %	2.19 %	3.46 %	4.95 %	3.24 %	1.78 %	0.93 %
POD	15.89 %	17.73 %	28.87 %	42.97 %	14.61 %	6.16 %	2.27 %
EIM	73.95 %	72.21 %	54.91 %	35.74 %	47.40 %	32.56 %	17.12 %
MapsIntra	8.36 %	7.87 %	12.76 %	16.33 %	34.73 %	59.47 %	79.65 %
MapsInter	0.01 %	0.01 %	0.01 %	0.01 %	0.02 %	0.03 %	0.03 %

Table 4.5: Run-time on the same computer as in Table 4.4 of the offline phases of the same reduced models as in Table 4.4, that is the reduced models are characterized by the common parameter $\epsilon_\mathcal{B} = 0.1$ and the varying parameter set $(N_\mathcal{B}, \epsilon_{POD}, \epsilon_{EI})$. 'Overall' gives the offline phases' overall duration measured in hours, 'SubdivSnaps' refers to the subdivision of the snapshots in order to produce $N_\mathcal{B}$ reduced basis sets, 'POD' to the POD procedures developing the approximation spaces for the phase-field and the chemical potential, 'EIM' to the EIM addressing the non-linearity of the high-dimensional phase-field equation (2.6)/(2.10), 'MapsIntra' refers to the pre-computation of the constant mappings used in the online phase in order to compute the reduced solutions, and 'MapsInter' refers to the pre-computation of the constant projection operators for basis change in the online phase.

field and chemical potential in the macroscopic node $(0,0)$. Contrary to that the errors of the smaller solids remain on nearly the same level throughout the whole time-interval. More probably than not this is due to the fact that the reduced model is constructed from snapshots which are mostly related to smaller solids. Nevertheless, all errors are smaller than the errors of the adaptive detailed model whose snapshots were used to construct the reduced model. Consequently, pre-selecting snapshots by the adaptive strategy has the desired effect: the offline phase is computed faster than without the pre-selection and the reduced model's accuracy is significantly greater than of the underlying adaptive detailed solution.

Table 4.5 tabulates the duration of the offline phases of the reduced models considered in the previous paragraph. Clearly, if $N_\mathcal{B}$ is fixed, the smaller the tolerances ϵ_{POD} of the POD-procedure and ϵ_{EI} of the EIM, the longer the duration of the offline phase. If ϵ_{POD} and ϵ_{EI} are fixed, then the larger the number $N_\mathcal{B}$ of the basis sets, the smaller the POD-procedures' and EIM's share in the overall duration of the offline phase, and contrariwise the larger the share of the procedure that pre-computes the constant mappings in the online phase. Since none of the offline phases takes more than 14 hours, the duration of all seven reduced models' offline phases is very acceptable.

Finally, the last Figures 4.5 and 4.6 of this subsection present results of the construction of the reduced model with parameters $N_\mathcal{B} = 100$, $\epsilon_{POD} = 1e\text{-}13$, $\epsilon_{EI} = 1e\text{-}5$ and $\epsilon_\mathcal{B} = 0.1$. The first figure shows that the different basis sets are responsible for different intervals of solid volumes: if a reduced solution's solid phase's volume is located in the specific interval
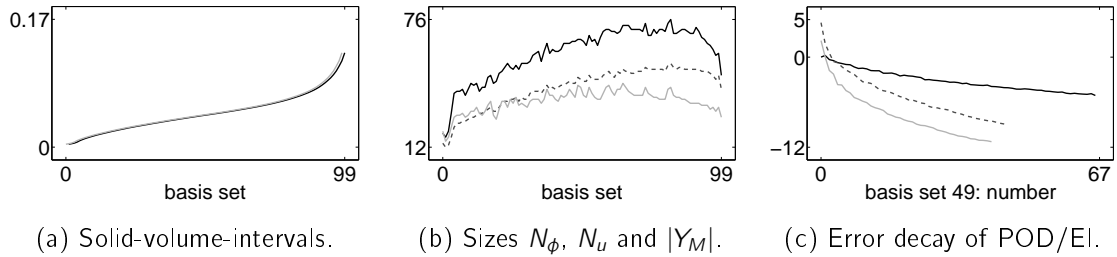
(a) Solid-volume-intervals.   (b) Sizes N_ϕ, N_u and $|Y_M|$.   (c) Error decay of POD/EI.

Figure 4.5: Results on the large time-space cylinder of the reduced model with parameters $N_B = 100$, $\epsilon_{POD} = 1e\text{-}13$, $\epsilon_{EI} = 1e\text{-}5$ and $\epsilon_B = 0.1$. Figure (a) depicts the maximum (light-gray) and minimum of the intervals of the volumes of the solid phases which are constructed by the different basis sets; basis set 0's minimum is zero and basis set 99 is not bounded from above, but the largest volume of the training data is only 0.1684. Figure (b) shows the sizes N_ϕ (dashed), N_u (light-gray) and $|Y_M|$ of the basis sets. And Figure (c) depicts for basis set 49 the decay of the $\log_{10}$ of the eigenvalues of the correlation operator of the underlying snapshots for the phase-field (dashed) and for the chemical potential (light-gray) and furthermore the decay of the error of the Empirical Interpolation Method for the increasing number of magic nodes.

of a basis set, then the reduced solution of the next step in time is constructed by this basis set. Furthermore, it indicates that the sizes of the basis sets are maximal for basis sets correlated to medium volume sizes, and that they differ significantly. These observations indicate that the partitioning method may be optimized. Finally, the figure describes for a sample basis set the decay of the eigenvalues of the two correlation operators of the snapshots for the phase-field and the chemical potential: those decays are rapid implying that the system comprises a strong ability to be compressed. The Figure 4.6 illustrates the differences of the basis sets: for example the location of the magic points moves from the center of the microscopic domain for basis sets related to small volumes to outer regions for larger volumes. This is due to the fact that, disregarding one point in $(0, 0)$, the magic points are always located in the phase transition zones of the microstructures. The inner-to-outer-movement holds also for the characteristic shapes of the principal modes of the POD-bases. The different sizes of the basis sets explain for example why it takes nearly twice as long to solve the reduced model in $(0, 0)$ as in $(19, 9)$: in course of the simulation all the basis sets are used to construct the solution in $(0, 0)$, but for $(19, 9)$ only the smaller basis sets.

In this subsection a reduced model with parameters $N_B = 100$, $\epsilon_{POD} = 1e\text{-}13$, $\epsilon_{EI} = 1e\text{-}5$, $\epsilon_B = 0.1$ was constructed that is very efficient: alongside accurate results, the model is solved in much less time than the detailed model. The next subsection is devoted to the macroscopic conditions that must be fulfilled such that the reduced model still delivers accurate results.

4.3   Generalization ability: variation of the macroscopic problem

The reduced model is constructed from microscopic solutions whose developments are manipulated by certain temperature evolutions. Hence, it can be expected that if a setting S produces temperature evolutions that are similar to the reduced model's training data evolutions, then the reduced solution is expected to be accurate for the setting S.
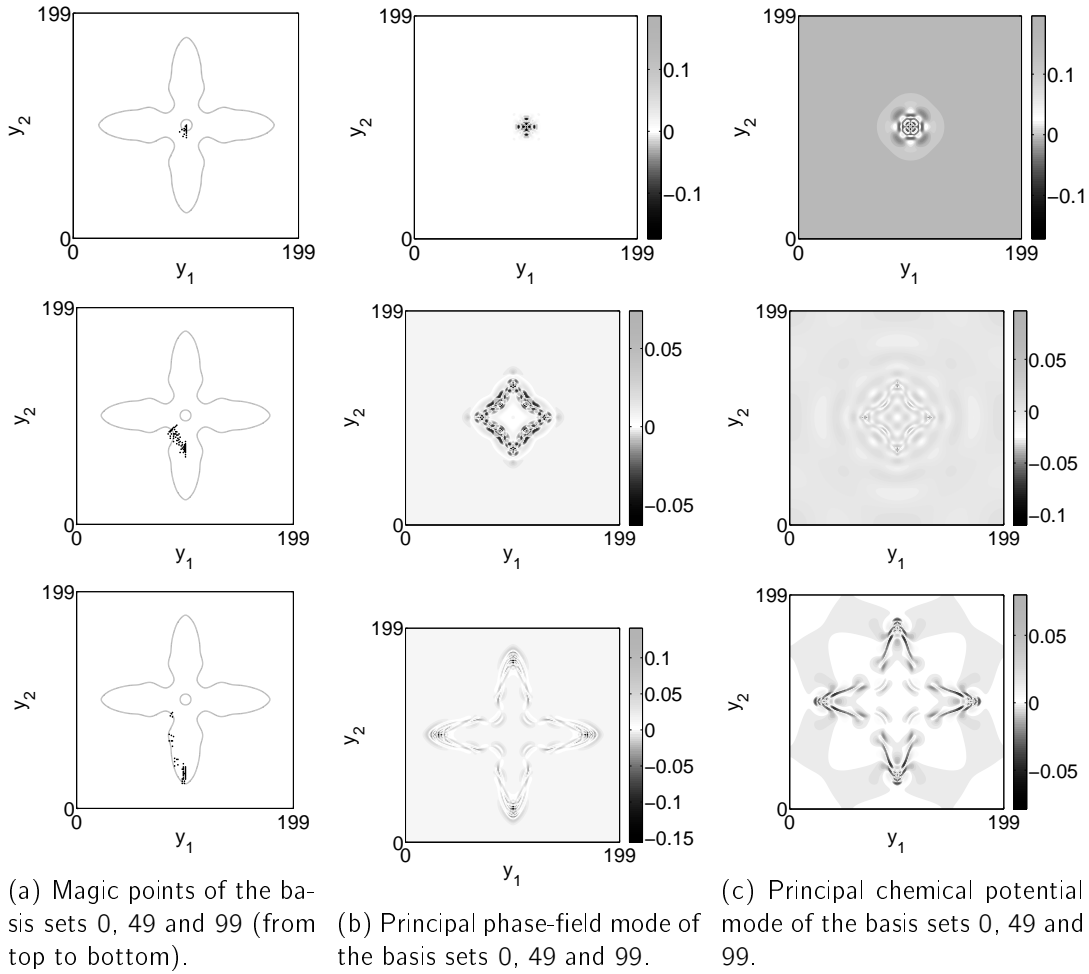
(a) Magic points of the basis sets 0, 49 and 99 (from top to bottom).

(b) Principal phase-field mode of the basis sets 0, 49 and 99.

(c) Principal chemical potential mode of the basis sets 0, 49 and 99.

Figure 4.6: Results on the large time-space cylinder of the reduced model with parameters $N_B = 100$, $\epsilon_{POD} = 1e\text{-}13$, $\epsilon_{EI} = 1e\text{-}5$ and $\epsilon_B = 0.1$. Figure (a) presents the distribution of the magic points on the microscopic domain for the basis sets 0, 49 and 99: dots mark the magic points, the inner circle represents the initial solid phase and the larger dendrite the largest solid phase of the training data. Figure (b) shows the principal mode of the POD-basis for the phase-field for the same basis sets and Figure (c) depicts the same for the chemical potential.

Table 4.6 specifies the parameters of three settings and the setting S_0 of the previous subsection used to construct the reduced model with parameters $N_B = 100$, $\epsilon_{POD} = 1e\text{-}13$, $\epsilon_{EI} = 1e\text{-}5$ and $\epsilon_B = 0.1$. In order to clarify the situation: the settings and the detailed but also the reduced solutions change, although the reduced model remains the same. Figure 4.7 illustrates the detailed macroscopic temperature solutions for the settings S_1, S_2 and S_3; the solution of S_0 is depicted in Figure 4.2. The shape of all solutions is similar, but the minimal temperature of S_1 is significantly smaller than of S_0 whose itself is significantly smaller than of S_2. This can also be deduced from the results presented in Table 4.7 comparing not only the detailed macroscopic temperature solutions of the settings S_0, S_1 and S_2 but also their microscopic phase-field solutions. Furthermore, for all settings the respective reduced is compared to the respective detailed solution.

Because the minimal temperature decreases faster over time for setting S_1 than for S_0 the largest dendrite of S_1 grows faster than of S_0 resulting in volumes of 0.2029

setting	$H_{g,1}$	$H_{g,2}$	$c_{\text{boundary-flux}}$	K
S_0	20	10	5e-6	200
S_1	20	10	6e-6	200
S_2	20	10	4e-6	200
S_3	50	20	7e-6	500

Table 4.6: *Generalization ability: variation of the macroscopic problem. Tabulated are the varying parameters of the macroscopic settings S_0, S_1, S_2 and S_3. Common to all of them are $H_\ell = 200$ and $K_t = 50000$.*
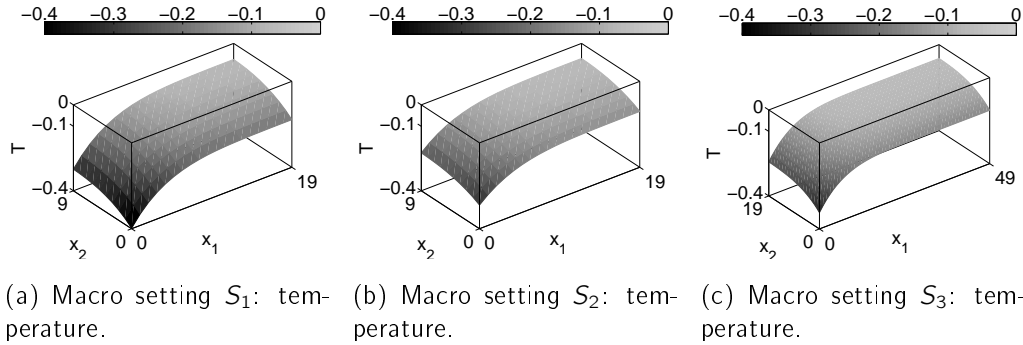

(a) Macro setting S_1: temperature. (b) Macro setting S_2: temperature. (c) Macro setting S_3: temperature.

Figure 4.7: *Generalization ability: variation of the macroscopic problem. The figures depict the final macroscopic temperature fields for the setting S_1, S_2 and S_3. The solution for S_0 is illustrated in Figure 4.2.*

difference	$\|\Delta T\|_{Q,\infty}$	$\|\Delta T\|_{Q,2}$	$\|\Delta\phi\|_{Q_1^\star,\infty}$	$\|\Delta\phi\|_{Q_2^\star,\infty}$	$\|\Delta\phi\|_{Q_3^\star,\infty}$	$\|\Delta\phi\|_{Q_4^\star,\infty}$
$r(S_0) - d(S_0)$	6.08e-5	2.15e-6	7.13e-4	1.21e-4	1.40e-4	8.40e-5
$d(S_1) - d(S_0)$	5.39e-2	1.21e-2	1.89e+0	1.04e+0	1.71e+0	6.09e-2
$r(S_1) - d(S_1)$	1.53e-1	2.12e-3	2.22e+0	1.25e-3	6.30e-2	8.40e-5
$d(S_2) - d(S_0)$	5.38e-2	1.23e-2	1.91e+0	1.05e+0	1.69e+0	6.16e-2
$r(S_2) - d(S_2)$	1.78e-3	3.27e-5	1.11e-1	7.56e-4	6.56e-3	8.40e-5
$r(S_3) - d(S_3)$	5.60e-3	4.68e-5	5.50e-1	5.79e-4	4.38e-3	4.90e-4

Table 4.7: *Generalization ability: variation of the macroscopic problem. Tabulated are the differences of the solutions of the macroscopic temperature and the microscopic phase-fields in the corner nodes of the macroscopic domain. For the macroscopic setting S_i the term $r(S_i)$ indicates the reduced and $d(S_i)$ the detailed solution. $Q_i^\star$ denotes for $i = 1, \ldots, 4$ the time-space cylinder $I_{t_{end}, k_t} \times \{x_i\} \times Y_{h_\ell}$ with $x_1 = (0,0)$, $x_2 = (H_{g,1}, 0)$, $x_3 = (0, H_{g,2})$ and $x_4 = (H_{g,1}, H_{g,2})$.*

and 0.1684 in the end. Consequently, as the training data does not contain the largest dendrites of S_1, they differ significantly: the most appropriate phase-field POD-basis is not appropriate enough to produce an accurate reduced approximation. For smaller dendrites the approximations are noteworthy better. The reduced solution for setting S_2 is much more accurate because the largest dendrite is only of volume 0.1344. Still, the error is not immaterial. The same holds for the setting S_3 with a larger macroscopic domain and a larger diffusivity K. At least the dendrites related to smaller volumes are approximated quite accurately.

Finally, Figure 4.8 presents results for the setting S_4, which is equal to S_3, only the heat

(a) Final detailed temperature.

(b) Difference $\phi_{\text{red}} - \phi_{\text{det}}$.
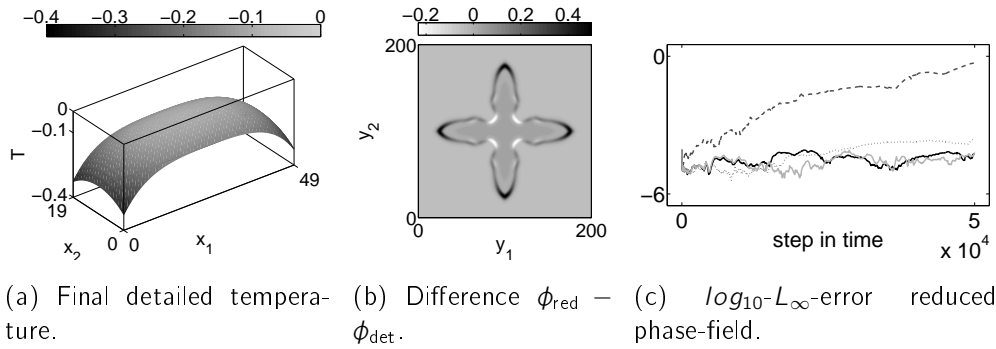
(c) log_{10}-L_∞-error reduced phase-field.

Figure 4.8: Generalization ability: variation of the macroscopic problem. The error of the reduced compared to the detailed temperature solution is $\|\Delta T\|_{Q,\infty} = 5.67e\text{-}3$ or rather $\|\Delta T\|_{Q,2} = 8.41e\text{-}5$. Figure (a) depicts the detailed temperature solution in the end, (b) the difference of the reduced and the detailed phase-field solution in the end in the macroscopic node $(0,0)$, and Figure (c) the log_{10} of the $L_\infty(Y)$-errors of the microscopic phase-fields in the macroscopic nodes $(0,0)$ (dashed), $(8,3)$ (dotted), $(16,6)$ (dark-gray) and $(24,9)$.

fluxes on the boundary of the macroscopic domain are different: it is $\frac{k_t K}{2h_g^2}\nabla T \cdot n = -1.4e\text{-}5$ for both vertical and $-7e\text{-}6$ for both horizontal boundaries in (4.1). In the end, the largest dendrite's volume is 0.1587 which is smaller than of the largest dendrite of setting S_1. Again, the reduced approximation of the smaller dendrites is accurate, but for the largest it is weak: the fingers of the dendrite are a little longer in the reduced but the body is a little smaller than in the detailed solution.

The numerical results presented in this section indicate that the correctness of the reduced model does, as expected, neither depend on the size of the macroscopic domain nor on the shape of the macroscopic temperature field. It is only the temperature evolutions influencing the microscopic problems in the online phase that are fundamental to precision. The closer they are to the offline evolutions influencing the training data, the more accurate is the reduced solution.

5 Conclusion and outlook

The combination of several modern procedures for treating time and parameter dependency as well as non-linearity induced a successful model reduction scheme for a nontrivial two-scale model. The complex reduced model comprises a full offline-online decomposition, hence its computational complexity is completely independent of the detailed discretization complexity. Minor new methodological contributions presented in this article are the solution of reduced systems via Least-Squares instead of Galerkin, and the partitioning approach adapted from problem specific feature extraction with projection-based basis change.

A possibility for extension would be an improved basis generation. As described, the number of snapshots for various trajectories is a problem in case of many time-steps and many nodes. Presumably, the POD-Greedy procedure developed in [17, 19] could be applied for the construction of provably quasi-optimal approximation spaces. Also the derivation of error estimators could be a possible future direction for the considered two-

scale model.

Acknowledgment

References

[1] F. Albrecht, B. Haasdonk, S. Kaulmann, and M. Ohlberger. The localized reduced basis multiscale method. In *Proc. of Algorithmy 2012*, 393–403, 2012.

[2] M. Barrault, Y. Maday, N.C. Nguyen, and A.T. Patera. An 'empirical interpolation' method: application to efficient reduced-basis discretization of partial differential equations. *C. R. Acad. Sci. Paris Series I*, 339:667–672, 2004.

[3] S. Boyaval. Reduced-basis approach for homogenization beyond the periodic setting. *Multiscale Model. Simul.*, 7(1):466–494, 2008.

[4] G. Caginalp. An analysis of a phase field model of a free boundary. *Arch. Ration. Mech. Anal.*, 92:205–245, 1986.

[5] S. Chaturantabut and D.C. Sorensen. Discrete empirical interpolation for nonlinear model reduction. *SIAM J. Sci. Comput.*, 32(5):2737–2764, 2010.

[6] D. Cioranescu and P. Donato. *An Introduction to Homogenization*. Oxford University Press, New York, 1999.

[7] S. Davis. *Theory of Solidification*. Cambridge University Press, Cambridge, 2001.

[8] M. Dihlmann, M. Drohmann, and B. Haasdonk. Model reduction of parametrized evolution problems using the reduced basis method with adaptive time-partitioning. In *Proc. of ADMOS 2011*, 2011.

[9] M. Drohmann, B. Haasdonk, and M. Ohlberger. Reduced basis approximation for nonlinear parametrized evolution equations based on empirical operator interpolation. *SIAM J. Sci. Comput.*, 34(2)(2):A937–A969, 2012.

[10] C. Eck. Analysis of a two-scale phase field model for liquid-solid phase transitions with equiaxed dendritic microstructure. *Multiscale Model. Simul.*, 3:28–49, 2004.

[11] C. Eck. Homogenization of a phase field model for binary mixtures. *Multiscale Model. Simul.*, 3:1–27, 2004.

[12] C. Eck. A two-scale phase field model for liquid-solid phase transitions of binary mixtures with dendritic microstructure. Professorial dissertation, Universität Erlangen-Nürnberg, 2004.

[13] C. Eck. Error estimates for a finite element discretization of a two-scale phase field model. *Multiscale Model. Simul.*, 6:1–26, 2007.

[14] J.L. Eftang, D. Knezevic, and A. Patera. An hp certified reduced basis method for parametrized parabolic partial differential equations. *Math. Comp. Model Dyn.*, 17:4:395–422, 2011.

[15] J.L. Eftang, A.T. Patera, and E.M. Rønquist. An hp certified reduced basis method for parametrized elliptic partial differential equations. *SIAM J. Sci Comp*, 32(6):3170–3200, 2010.

[16] J.L. Eftang and B. Stamm. Parameter multi-domain "hp" empirical interpolation. *Internat. J. Numer. Methods Engrg.*, 90(4):412–428, 2012.

[17] B. Haasdonk. Convergence rates of the POD-Greedy method. *M2AN Math. Model. Numer. Anal.*, 47:859–873, 2013.

[18] B. Haasdonk, M. Dihlmann, and M. Ohlberger. A training set and multiple basis generation approach for parametrized model reduction based on adaptive grids in parameter space. *Math. Comp. Model Dyn.*, 17:423–442, 2012.

[19] B. Haasdonk and M. Ohlberger. Reduced basis method for finite volume approximations of parametrized linear evolution equations. *Math. Model. Numer. Anal.*, 42(2):277–302, 2008.

[20] U. Hornung, editor. *Homogenization and Porous Media*. Springer, New York, 1997.

[21] T.Y. Hou and X.-H. Wu. A multiscale finite element method for elliptic problems in composite materials and porous media. *J. Comp. Phys.*, 134:169–189, 1997.

[22] V.V. Jikov, S.M. Kozlov, and O.A. Oleinik. *Homogenization of Differential Operators and Integral Functionals*. Springer, Berlin, 1994.

[23] I.T. Jolliffe. *Principal Component Analysis*. Springer-Verlag, 2002.

[24] S. Kaulmann, M. Ohlberger, and B. Haasdonk. A new local reduced basis discontinuous Galerkin approach for heterogeneous multiscale problems. *Comp. Ren. Mathem.*, 349(23-24):1233–1238, 2011.

[25] D.J. Knezevic and A.T. Patera. A certified reduced basis method for the Fokker–Planck equation of dilute polymeric fluids: Fene dumbbells in extensional flow. *SIAM J. Sci. Comput.*, 32(2):793–817, 2010.

[26] R. Kobayashi. Modeling and numerical simulations of dendritic crystal growth. *Phys. D*, 63:410–423, 1993.

[27] W. Kurz and D.J. Fisher. *Fundamentals of Solidification*. TransTech Publications, Switzerland, 1998.

[28] Y. Maday, N. C. Nguyen, A. T. Patera, and G. S. H. Pau. A general multipurpose interpolation procedure: the magic points. *CPAA*, 8(1):383–404, 2009.

[29] N.C. Nguyen. A multiscale reduced-basis method for parametrized elliptic partial differential equations with multiple scales. *J. Comp. Phys.*, 227(23):9807–9822, 2008.

[30] B. Peherstorfer, D. Butnaru, K. Willcox, and H. Bungartz. Localized Discrete Empirical Interpolation Method. Technical Report TR-13-1, Aerospace Computational Design Lab, Dept. of Aeronautics & Astronautics, MIT, June 2013.

[31] M. Redeker and C. Eck. A fast and accurate adaptive solution strategy for two-scale models with continuous inter-scale dependencies. *J. Comp. Phys.*, 240:268–283, 2013.

[32] L. Tan and N. Zabaras. Multiscale modeling of alloy solidification using a database approach. *J. Comp. Phys.*, 227:728–754, 2007.

[33] H.H. Viet and C. Schwab. High-dimensional finite elements for elliptic problems with multiple scales. *Multiscale Model. Simul.*, 3:168–194, 2005.

[34] A. Visintin. *Models of Phase Transitions*. Birkhäuser, Boston, 1996.

[35] S. Volkwein. *Lecture Notes: Proper Orthogonal Decomposition: Theory and Reduced-Order Modelling*. University of Constance, 2013.

[36] E W. and B. Engquist. The heterogeneous multiscale method. *Commun. Math. Sci.*, 1:87–123, 2003.

[37] B. Wieland. *Reduced Basis Methods for Partial Differential Equations with Stochastic Influences*. PhD Thesis, Universität Ulm, April 2013.